

# Kozai–Lidov oscillations triggered by a tilt instability of detached circumplanetary discs

Rebecca G. Martin<sup>1\*</sup>, Zhaohuan Zhu<sup>1</sup>, Philip J. Armitage<sup>2,3</sup>, Chao-Chin Yang<sup>1</sup>  
and Hans Baehr<sup>1</sup>

<sup>1</sup>*Department of Physics and Astronomy, University of Nevada, Las Vegas, 4505 South Maryland Parkway, Las Vegas, NV 89154, USA*

<sup>2</sup>*Center for Computational Astrophysics, Flatiron Institute, New York, NY 10010, USA*

<sup>3</sup>*Department of Physics and Astronomy, Stony Brook University, Stony Brook, NY 11794, USA*

## ABSTRACT

Circumplanetary discs can be linearly unstable to the growth of disc tilt in the tidal potential of the star-planet system. We use three-dimensional hydrodynamical simulations to characterize the disc conditions needed for instability, together with its long term evolution. Tilt growth occurs for disc aspect ratios, evaluated near the disc outer edge, of  $H/r \gtrsim 0.05$ , with a weak dependence on viscosity in the wave-like regime of warp propagation. Lower mass giant planets are more likely to have circumplanetary discs that satisfy the conditions for instability. We show that the tilt instability can excite the inclination to above the threshold where the circumplanetary disc becomes unstable to Kozai–Lidov (KL) oscillations. Dissipation in the Kozai–Lidov unstable regime caps further tilt growth, but the disc experiences large oscillations in both inclination and eccentricity. Planetary accretion occurs in episodic accretion events. We discuss implications of the joint tilt–KL instability for the detectability of circumplanetary discs, for the obliquity evolution of forming giant planets, and for the formation of satellite systems.

**Key words:** accretion, accretion discs – hydrodynamics – instabilities – planets and satellites: formation – planetary systems – stars: pre-main sequence

## 1 INTRODUCTION

A planet that forms in a protoplanetary disc is able to tidally open a gap in the protoplanetary disc when it reaches the mass of Neptune (Lin & Papaloizou 1986; D’Angelo et al. 2002; Bate et al. 2003; Ayliffe & Bate 2009a,b). Material continues to flow from the circumstellar disc into the gap towards the planet (Artymowicz & Lubow 1996). Since the planet has a size that is much smaller than the Hill radius, a circumplanetary disc forms (Lubow et al. 1999; D’Angelo et al. 2002). The study of circumplanetary discs is important for a number of reasons. First, most of the mass of Jupiter may have been accreted from a circumplanetary disc. Thus, the dynamics of a circumplanetary disc may have a major influence on the properties of the forming planet. Secondly, regular satellites, those that have orbits that are close to coplanar to the equatorial plane of the planet and low orbital eccentricities, are thought to form in circumplanetary discs (e.g. Lunine & Stevenson 1982; Canup & Ward 2002; Mosqueira & Estrada 2003; Batygin & Morbidelli 2020). Finally, circumplanetary discs may provide observational signatures of forming planets (Zhu 2015).

Misaligned circumplanetary discs may change the obliquity

of a forming planet through both the accretion of misaligned material and the torque acting to align the planet spin to the disc (Martin et al. 2020). In the solar system, Saturn, Uranus and Neptune have large obliquities and their regular satellites and ring systems are almost aligned with the spin of each planet. Processes that occur after satellite formation can also lead to planet spin-orbit misalignment such as giant impacts (Safronov 1966; Benz et al. 1989; Morbidelli et al. 2012), spin-orbit resonances (Ward & Hamilton 2004; Vokrouhlický & Nesvorný 2015; Brasser & Lee 2015; Rogoszinski & Hamilton 2020) and planet-circumstellar disc interactions (Millholland & Batygin 2019). A planet with a misaligned circumplanetary disc or a ring system would have deep transit. Some very low density planets that have been observed in this way (Masuda 2014; Jontof-Hutter et al. 2014) could be planets with misaligned discs or rings (Piro & Vissapragada 2020; Akinsanmi et al. 2020).

In Martin et al. (2020) we found that the large disc aspect ratio and tidally truncated size of circumplanetary discs means they are unstable to tilting through interaction with the tidal potential. Lubow (1992) first identified tilt instabilities in tidally distorted discs. We assume that accretion onto the circumplanetary disc (that has been examined by, for example by Tanigawa et al. 2012; Szulágyi et al. 2014; Schulik et al. 2020) can be ignored. This may occur, first, at the end of the lifetime of the circumstellar disc, when

\* E-mail: rebecca.martin@unlv.edu

there is no further replenishment as the circumstellar disc has been accreted on to the star or photoevaporated (e.g. [Clarke et al. 2001](#); [Alexander et al. 2006](#); [Owen et al. 2011](#)). Secondly, this may occur if a wide gap is induced by a massive planet in an inviscid disc (e.g. [Lin & Papaloizou 1986](#)) or in a system with multiple planets (e.g. [Zhu et al. 2011](#)). Stochastic accretion of gas from the turbulent protoplanetary disc ([Gressel et al. 2013](#)) may provide the small initial tilt that is needed for the disc to be unstable to tilting.

In this work, we study the interaction between the tilt instability and Kozai–Lidov (KL, [Kozai 1962](#); [Lidov 1962](#)) oscillations of inclination and eccentricity, which can occur in both point-mass ([Naoz 2016](#)) and fluid disc ([Martin et al. 2014](#); [Fu et al. 2015a,b](#); [Franchini et al. 2019](#)) systems. KL dynamics become important above a critical inclination. For a test particle this inclination is about  $39^\circ$  but for a disc it depends upon the disc aspect ratio ([Lubow & Ogilvie 2017](#); [Zanazzi & Lai 2017](#)). Moderately tilted discs may then see their tilts increase due to the tilt instability, before entering a regime in which both the tilt and KL instabilities are active. In Section 2 we discuss the results of SPH simulations of detached circumplanetary discs. In Section 3 we discuss some effects that were neglected in our simulations and their effects on the evolution. In Section 4 we discuss implications of our results on giant planet formation, regular satellite formation and observations of forming planets. We conclude in Section 5.

## 2 HYDRODYNAMICAL SIMULATIONS

We use the smoothed particle hydrodynamics (SPH) code PHANTOM ([Price & Federrath 2010](#); [Lodato & Price 2010](#); [Price et al. 2018](#)) to model a detached circumplanetary disc that is misaligned to the planet orbit. PHANTOM has been used extensively to model misaligned discs in binary systems (e.g. [Nixon 2012](#); [Nixon et al. 2013](#); [Smallwood et al. 2019](#); [Franchini et al. 2020](#); [Bi et al. 2020](#)). There are two sink particles (e.g. [Bate et al. 1995](#)), one representing the star with mass  $M_s$  and the other representing the planet with mass  $M_p = 10^{-3} M_s$ . The simulations do not depend on the orbital separation of the planet,  $a$ , because all lengths are scaled to the Hill radius given by

$$r_H = a \left( \frac{M_p}{3M_s} \right)^{1/3}. \quad (1)$$

We choose the accretion radius of the star to be  $1.4 r_H$ , and that of the planet is  $0.03 r_H$  ([Martin et al. 2020](#)). Any particle that moves within the accretion radius is accreted on to the sink. The mass and angular momentum of the accreted particle are added to the sink so that mass, linear momentum and angular momentum are conserved. The planet is in a circular orbit with orbital period  $P_{\text{orb}} = 2\pi / \sqrt{G(M_p + M_s)/a^3}$ .

The simulation parameters are summarised in Table 1. The surface density of the disc is initially distributed as  $\Sigma \propto r^{-3/2}$  between the inner radius of  $r_{\text{in}} = 0.03 r_H$  up to the outer radius of  $r_{\text{out}} = 0.4 r_H$ . Because the density evolves quickly, the initial truncation radii of the disc do not significantly affect the disc evolution. The initial outer truncation radius is approximately the size of a tidally truncated circumplanetary disc ([Martin & Lubow 2011](#)), although the truncation radius of a misaligned disc may be larger ([Lubow et al. 2015](#); [Miranda & Lai 2015](#)). There is no addition of material to the disc during the simulation. We do not include disc self-gravity and so the mass of the disc does not affect the disc dynamics. We discuss this assumption further in Section 3. The initial total disc mass is small compared to the planet mass,

$M_{\text{d0}} = 10^{-6} M_s$ . This is about the maximum steady state disc mass found in two-dimensional hydrodynamic simulations for various disc parameters with infall accretion rates up to  $10^{-9} M_\odot \text{yr}^{-1}$  ([Chen et al. 2021](#)). The tidal torque from the Sun excites spiral density waves that result in shocks that transport angular momentum through the disc even in the absence of other sources of viscosity ([Zhu et al. 2016](#)).

The disc is initially inclined to the orbital plane of the planet with inclination  $i_0$ . We consider three different initial tilt angles,  $i_0 = 10^\circ$ ,  $i_0 = 30^\circ$  and  $i_0 = 60^\circ$ . Small tilt angles, up to about  $15^\circ$  may be expected during the formation of a circumplanetary disc due to stochastic accretion flow into the planet Hill sphere ([Gressel et al. 2013](#)). While we do not expect the disc to form with larger initial tilt, we consider larger values that may be achieved because of the tilt instability ([Martin et al. 2020](#)). The long term effects and some caveats are discussed in Section 3 in more detail.

The disc is locally isothermal with fixed sound speed  $c_s \propto r^{-q}$ . Typically we take  $q = 0.75$  so that  $\alpha$  and the smoothing length  $\langle h \rangle / H$  are constant over the disc ([Lodato & Pringle 2007](#)) although we consider one simulation with  $q = 0.5$  (constant disc aspect ratio). We generally take the [Shakura & Sunyaev \(1973\)](#)  $\alpha$  parameter to be 0.01 although we consider one simulation with a smaller  $\alpha = 0.005$ . The disc viscosity is implemented by adapting the SPH artificial viscosity according to the procedure described in [Lodato & Price \(2010\)](#) with  $\alpha_{\text{AV}}$  shown in column 5 of Table 1 and  $\beta_{\text{AV}} = 2$ . The circumplanetary disc is initially resolved with shell-averaged smoothing length per scale height shown in column 4 of Table 1.

In order to analyse the simulations we divide the particles into 100 bins that are linear in spherical radius. The bins extend from the innermost particle around the planet to the outermost particle that is bound to the planet. Within each bin we calculate the mean values for the surface density,  $\Sigma$ , the disc inclination with respect to the planet orbital plane,  $i$ , the disc nodal phase angle (longitude of the ascending node),  $\phi$ , the disc eccentricity,  $e$ , and the disc argument of periapsis,  $\phi_e$ .

We define the tilt growth timescale of the disc as

$$t_{\text{growth}} = \frac{i}{di/dt}. \quad (2)$$

We approximate the growth timescale by calculating a least squares quartic polynomial fit to the inclination of the disc in time. In Table 1 we show the growth timescale at  $t = 10 P_{\text{orb}}$  for simulations in which the disc is not undergoing KL oscillations at that point. Simulations with an initial inclination of  $i_0 = 10^\circ$  are fit up to time  $t = 40 P_{\text{orb}}$ , simulations with an initial inclination of  $i_0 = 30^\circ$  are fit up to a time of  $t = 30 P_{\text{orb}}$ , while simulations with an initial inclination of  $i_0 = 60^\circ$  are fit up to a time of  $t = 12 P_{\text{orb}}$ . After these time intervals the discs may undergo KL oscillations.

### 2.1 Mildly inclined circumplanetary discs

Two components of the tidal potential determine the dynamics of a mildly misaligned disc. Retrograde nodal precession is caused by the  $m = 0$  component. In the wave-like regime, where  $\alpha < H/r$ , the disc holds itself together through wave-like communication ([Papaloizou & Pringle 1983](#)) and this leads to solid body nodal precession ([Papaloizou & Terquem 1995](#); [Larwood et al. 1996](#); [Terquem 1998](#)). An ‘‘oscillating’’ torque with a period of half the orbital period is produced by the  $m = 2$  component of the torque. This does not change the mean precession rate ([Katz et al. 1982](#)). Dissipation within the disc means that the  $m = 0$  component leads the

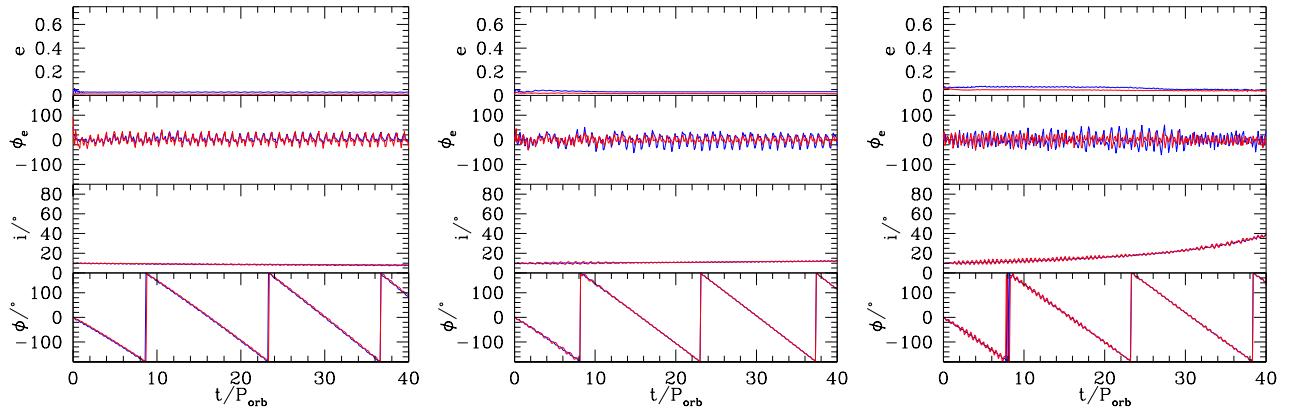


**Figure 1.** Hydrodynamical simulations of a circumplanetary disc with initial inclination of  $i_0 = 10^\circ$  with disc aspect ratio  $(H/r)_{\text{out}} = 0.025$  (left, run1),  $(H/r)_{\text{out}} = 0.05$  (middle, run2) and  $(H/r)_{\text{out}} = 0.1$  (right, run3). The upper panel shows the eccentricity of the disc, the second panel shows the argument of periaapsis, the third panel shows the inclination of the disc and the lower panel shows the nodal phase angle. The red lines show the disc orbital properties at radius  $r = 0.2 r_H$  and the blue lines at  $r = 0.3 r_H$ .

Simulation	Figure	$N$	$\langle h \rangle / H$	$\alpha_{\text{AV}}$	$q$	$(H/r)_{\text{in}}$	$(H/r)_{\text{out}}$	$i_0 / ^\circ$	$t_{\text{growth}}(10 P_{\text{orb}}) / P_{\text{orb}}$	KL
run1	1	500,000	0.60	0.17	0.75	0.05	0.025	10	-147	No
run2	1	500,000	0.37	0.27	0.75	0.1	0.05	10	204	No
run3	1	1,000,000	0.17	0.58	0.75	0.2	0.1	10	39	No
run4	4	500,000	0.25	0.39	0.5	0.1	0.1	10	51	No
run5	5	500,000	0.59	0.17	0.75	0.05	0.025	30	-232	No
run6	5	500,000	0.37	0.27	0.75	0.1	0.05	30	257	No
run7	5	1,000,000	0.19	0.53	0.75	0.2	0.1	30	43	No → Yes
run8	6	500,000	0.58	0.17	0.75	0.05	0.025	60	-	Yes
run9	6	500,000	0.37	0.27	0.75	0.1	0.05	60	-	Yes
run10	6	1,000,000	0.18	0.54	0.75	0.2	0.1	60	72	No → Yes
run11	7	1,000,000	0.18	0.27	0.75	0.2	0.1	60	80	No → Yes

**Table 1.** Parameters of the SPH simulations. The first column is the name of the simulation. The second column shows which Figure the simulation appears in. The third column is the initial number of particles in the simulation. The fourth column is the initial mass averaged smoothing length divided by the disc scale height. The fifth column is the artificial viscosity parameter. The sixth column is the sound speed index,  $c_s \propto r^{-q}$ . The seventh column is the disc aspect ratio at the disc inner edge. The eighth column is the disc aspect ratio at the initial disc outer radius. The ninth column is the initial disc inclination. The tenth column shows the disc tilt growth timescale at time  $t = 10 P_{\text{orb}}$ . The eleventh column describes whether the disc is unstable to KL oscillations.

disc to move towards coplanar alignment where the disc is aligned to the orbital plane of the planet. The  $m = 2$  term on the other hand leads to the tilt increasing (Lubow 1992; Lubow & Ogilvie 2000; Bate et al. 2000). For circumstellar discs, the outcome is normally coplanar alignment. However, because of the tidally truncated size of circumplanetary discs and their typically larger disc aspect ratio, their tilt tends to increase (Martin et al. 2020).

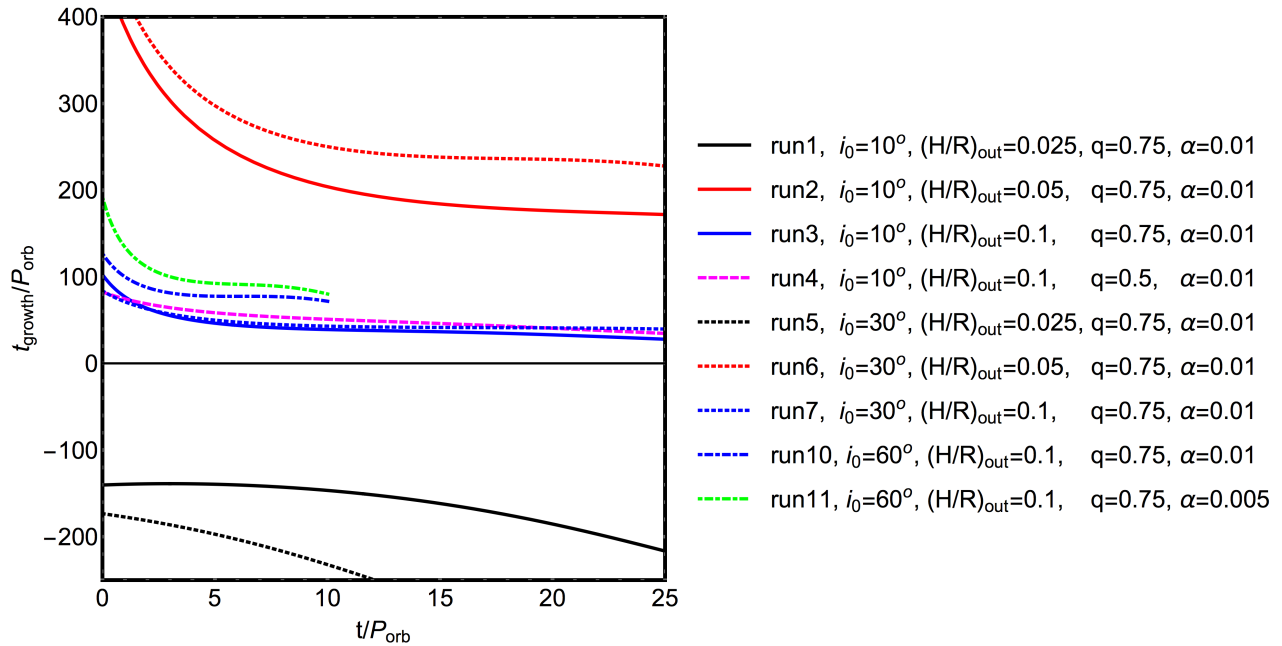
Fig. 1 shows three SPH simulations that begin with an initial disc inclination of  $i_0 = 10^\circ$  for different disc aspect ratios. The sound speed power law in each case has  $q = 0.75$  meaning that  $H/r \propto r^{-1/4}$ . The value of  $H/r$  at the initial disc outer edge,  $(H/r)_{\text{out}} = H/r(r = r_{\text{out}})$ , is about half the value at the inner edge,  $(H/r)_{\text{in}} = H/r(r = r_{\text{in}})$ . Each panel shows the disc eccentricity, the disc argument of periaapsis, the disc inclination and the disc nodal phase angle from top to bottom. Within each panel the red lines show the evolution in the middle of the disc at a radius  $r = 0.2 r_H$  while the blue lines show the evolution further out at  $r = 0.3 r_H$ .

The left panel of Fig. 1 shows the lowest disc aspect ratio considered,  $(H/r)_{\text{out}} = 0.025$  (run1). The disc in this simulation nodally

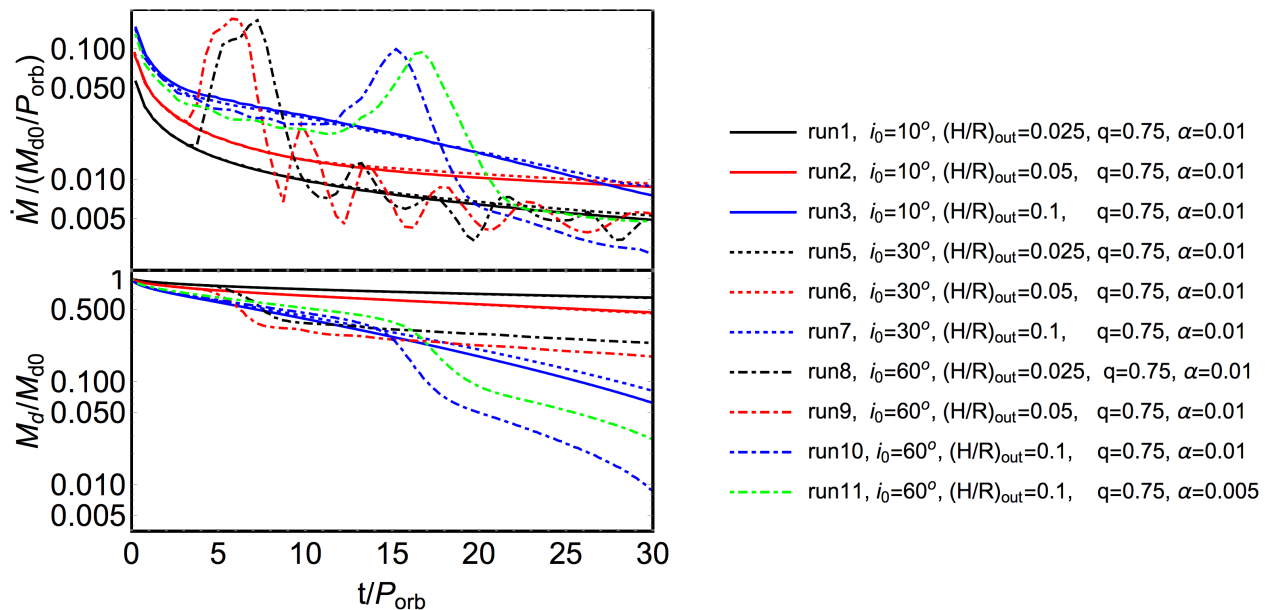
precesses at a roughly constant rate on a timescale of about  $18 P_{\text{orb}}$ . The tilt shows a slow decay. Since the red and the blue lines are very similar, the disc is precessing globally. The middle panel shows a higher disc aspect ratio of  $(H/r)_{\text{out}} = 0.05$  (run2). The tilt grows in this simulation. The right hand panel shows the SPH simulation presented in Martin et al. (2020) that has  $(H/r)_{\text{out}} = 0.1$  (run3). The disc tilt grows on a shorter timescale for larger disc aspect ratio. There is no eccentricity growth in any of these low initial tilt simulations.

Fig. 2 shows the tilt growth timescale (equation 2) as a function of time. Positive values represent discs with increasing tilts while negative values represent those with decreasing tilts. The three solid lines show the mildly misaligned simulations with  $i_0 = 10^\circ$  and  $q = 0.75$  for the three different disc aspect ratios  $(H/r)_{\text{out}} = 0.025$  (run1, black),  $(H/r)_{\text{out}} = 0.05$  (run2, red) and  $(H/r)_{\text{out}} = 0.1$  (run3, blue). For the simulations with increasing tilts (positive  $t_{\text{growth}}$ ), the growth timescale decreases over time but reaches a quasi-steady value.

Fig. 3 shows the time averaged accretion rate on to the planet



**Figure 2.** The approximate tilt growth timescale as a function of time for circumplanetary discs with initial misalignment  $i_0 = 10^\circ$  (solid and dashed lines),  $i_0 = 30^\circ$  (dotted lines) and  $i_0 = 60^\circ$  (dot-dashed lines). All lines have  $q = 0.75$  except the magenta dashed line which has  $q = 0.5$  and  $H/r = 0.1$ . All lines have  $\alpha = 0.01$  except the green line that has  $\alpha = 0.005$ . The disc aspect ratio is  $(H/r)_{\text{out}} = 0.025$  (black lines),  $(H/r)_{\text{out}} = 0.05$  (red lines) and  $(H/r)_{\text{out}} = 0.1$  (blue, magenta and green lines).



**Figure 3.** Time averaged accretion rate on to the planet (upper panel) and the mass of the disc (lower panel). The black lines show simulations with  $(H/r)_{\text{out}} = 0.025$ , the red lines show simulations with  $(H/r)_{\text{out}} = 0.05$  and the blue lines show simulations with  $(H/r)_{\text{out}} = 0.1$ . All the simulations have  $\alpha = 0.01$  except the green dot-dashed line that has  $\alpha = 0.005$  and  $(H/r)_{\text{out}} = 0.1$ . The solid lines have initial inclination  $i_0 = 10^\circ$ , the dotted lines have  $i_0 = 30^\circ$  and the dot-dashed lines have  $i_0 = 60^\circ$ .

and the disc mass. The solid lines show the simulations that are initially misaligned by  $i_0 = 10^\circ$  with  $q = 0.75$ . The lower the disc aspect ratio the slower the accretion on to the planet since the viscosity is lower. The accretion rate on to the planet decreases in time because the mass in the circumplanetary disc decreases.

### 2.1.1 Effect of the temperature structure

Fig. 4 shows the same simulation as in Fig. 1 but with a disc aspect ratio that is constant with radius ( $q = 0.5$ ) and  $H/r = 0.1$  (run4). The disc evolution is similar to the right hand panel of Fig. 1 which has  $(H/r)_{\text{out}} = 0.1$  (run3). The dashed magenta line in Fig. 2 shows the tilt growth timescale for the simulation with  $i_0 = 10^\circ$



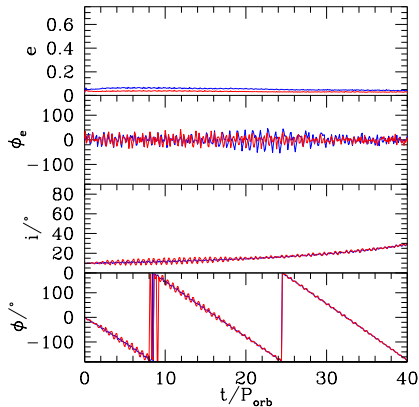


**Figure 4.** Same as the right panel of Fig. 1 (run3) except  $q = 0.5$  (run4). Simulations run3 and run4 have the same disc aspect ratio  $(H/r)_{\text{out}} = 0.1$ .

and  $q = 0.5$  is most similar to the simulation with the same initial inclination and  $(H/r)_{\text{out}}$  but  $q = 0.75$  (solid blue line, run3). Thus, the disc aspect ratio at the outer disc edge is what determines the disc evolution (not the disc aspect ratio in the inner parts of the disc) and the results are relatively insensitive to  $q$ . For more realistic temperature structures (than our standard choice) we expect the aspect ratio at the outer disc edge to determine the tilt growth timescale.

## 2.2 Moderately inclined circumplanetary discs

Fig. 5 shows simulations with a higher initial inclination of  $i_0 = 30^\circ$ . Similarly to the mildly misaligned discs, the tilt of the two larger disc aspect ratio discs increase while the tilt of the disc with lowest aspect ratio decreases. The tilt of the disc with the largest aspect ratio increases rapidly until it becomes unstable to KL oscillations above an inclination of about  $60^\circ$ . During the KL oscillation the disc eccentricity and inclination are exchanged. The lower panels of Fig. 5 show the disc in each simulation at a time of  $18 P_{\text{orb}}$ . In each case the disc is tilted but there is no eccentricity growth at this time.

The tilt growth timescales for these simulations are shown by the dotted lines in Fig. 2. The three different disc aspect ratios are  $(H/r)_{\text{out}} = 0.025$  (run5, black),  $(H/r)_{\text{out}} = 0.05$  (run6, red) and  $(H/r)_{\text{out}} = 0.1$  (run7, blue). The tilt growth timescale is sensitive to the disc aspect ratio and weakly dependent on the initial disc tilt. The tilt growth timescale increases with initial disc tilt.

The accretion rates for these simulations are shown in the dotted lines in Fig. 3. The accretion rates are very similar to those of the lower initial inclination discs (solid lines). However, when the disc undergoes a KL oscillation, the disc eccentricity leads to a higher accretion rate and also a higher rate of ejection of particles from the disc (e.g. Franchini et al. 2019). We cannot run the simulations for longer than shown as we lose resolution in the disc. In order to explore the behaviour further we next consider an even higher initial disc misalignment.

## 2.3 Highly inclined circumplanetary discs

Fig. 6 shows the evolution of discs that begin with an even higher initial inclination of  $i_0 = 60^\circ$ . The discs with lower disc aspect ratio are already unstable to KL oscillations at this inclination. The KL oscillations lead to a relatively quick alignment of the disc to

an inclination of about  $40^\circ$ . This is a result of dissipation within the disc due to the viscosity and because shocks form during the oscillations (Martin et al. 2014). A disc undergoes KL oscillations above a critical inclination that depends upon the disc aspect ratio (Lubow & Ogilvie 2017; Zanazzi & Lai 2017). The largest disc aspect ratio,  $(H/r)_{\text{out}} = 0.1$ , is not initially unstable at this inclination. However, since the inclination increases due to the tilt instability, it becomes unstable later in the simulation. During the KL oscillation the inclination of the disc decreases. The disc becomes stable again. The tilt instability again operates increasing the tilt until it becomes unstable again as seen by the eccentricity growth near the end of the simulation. Thus, the tilt instability is able to increase the range of initial disc tilts that are unstable to KL oscillations.

The tilt growth timescale of the simulation with  $(H/r)_{\text{out}} = 0.1$  (run10) is shown in the blue dot-dashed line in Fig. 2, until the time that the disc becomes KL unstable. The growth timescale is similar to the discs at lower inclination with the same disc structure (the other blue lines). The growth timescale for the simulations with lower  $(H/r)_{\text{out}}$  (run8 and run9) are not shown because they already undergo KL oscillations from the start.

The accretion rates on to the planets in the highly misaligned simulations are shown in the dot-dashed lines in Fig. 3. The KL oscillations lead to a significantly higher accretion rate on to the planet during the highly eccentric disc phase.

The simulations show that the nodal phase angles remain roughly constant with disc radius during the precession. However, the argument of periastron varies significantly over the radial extent of the disc. This is also clear in the lower panels of Fig. 6. The eccentricity vector of the inner hole in each case is not in the same direction as the eccentricity vector of the outer parts of the disc. This behaviour was seen before in protoplanetary disc simulations (e.g. Martin et al. 2014; Fu et al. 2015a,b; Franchini et al. 2019).

### 2.3.1 Effect of disc viscosity

Modelling of protoplanetary discs has been used to infer values of  $\alpha$  in the range  $10^{-4} - 10^{-2}$  (e.g. Hartmann et al. 1998; Andrews et al. 2009; Hueso & Guillot 2005; Flaherty et al. 2015; Rafikov 2016; Pinte et al. 2016; Flaherty et al. 2017; Ansdell et al. 2018; Flaherty et al. 2018, 2020). For circumplanetary discs similar observations are lacking, and the only current constraints are derived from models of satellite formation (e.g. Canup & Ward 2002; Lubow & Martin 2013). However, in general terms we expect that both circumplanetary discs and protoplanetary discs may contain a dead zone, a region where the magnetorotational instability (MRI) is inefficient at generating turbulence (Gammie 1996). The corresponding  $\alpha$  may therefore be low in circumplanetary discs (Lubow & Martin 2012, 2013; Fujii et al. 2014). The total rate of angular momentum transport in circumplanetary discs may, however, be larger than that in protoplanetary discs because spiral shocks transport angular momentum with an effective  $\alpha$  parameter in the range 0.001-0.02 (Zhu et al. 2016).

All of the simulations considered so far have assumed that  $\alpha = 0.01$ . To test the sensitivity of the results to this assumption we also consider a simulation with a lower viscosity parameter,  $\alpha = 0.005$  (run11). The lower viscosity leads to a longer viscous timescale and so we can follow the disc evolution for longer with better resolution. Fig. 7 shows the evolution of the disc. The dynamics of the disc are not strongly affected by  $\alpha$  as seen by comparing this to the right hand panel of Fig. 6 (run10) that has  $\alpha = 0.01$  and otherwise the same parameters. The green dot-dashed lines in Fig. 3 show the accretion rate on to the planet and the disc mass for

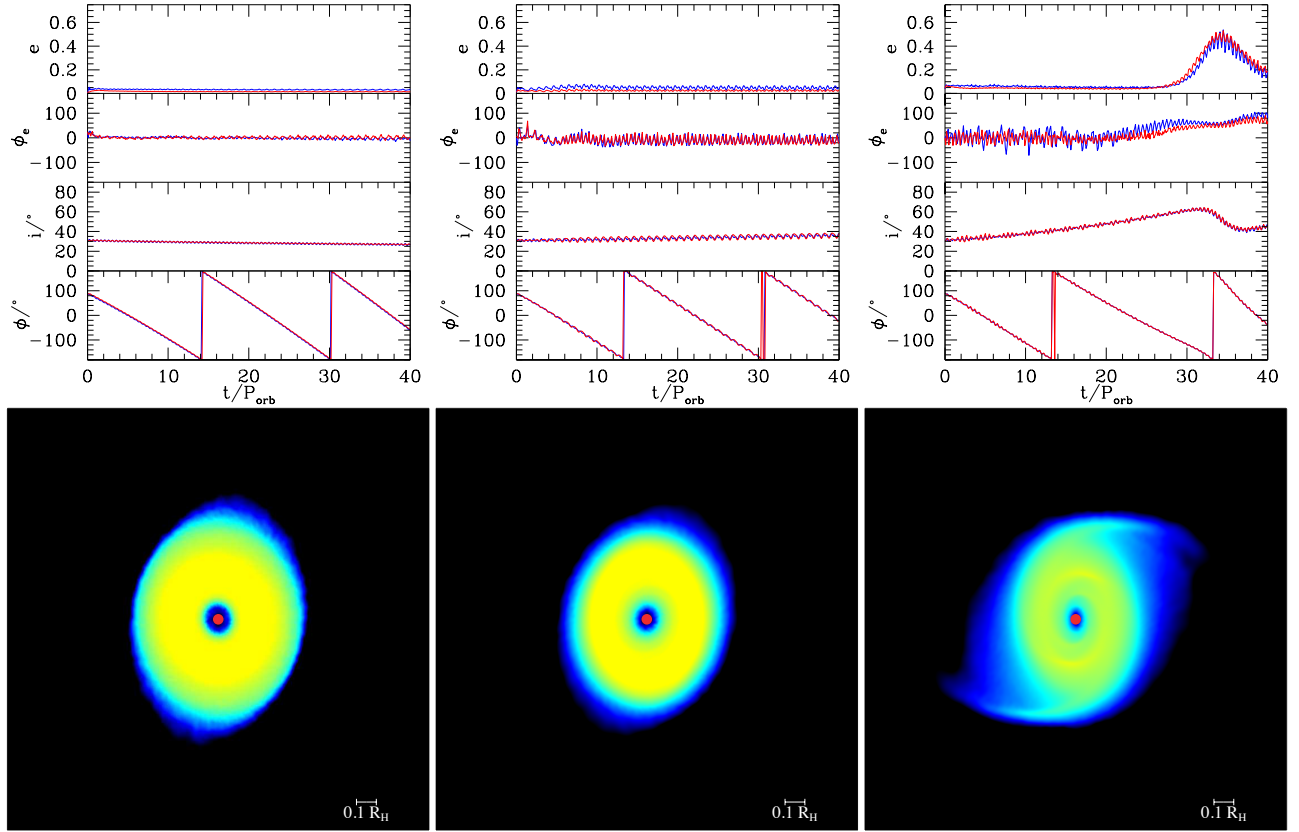


**Figure 5.** The upper panels are the same as Fig. 1 except the initial inclination is  $i_0 = 30^\circ$  with disc aspect ratios of  $(H/r)_{\text{out}} = 0.025$  (left, run5),  $(H/r)_{\text{out}} = 0.05$  (middle, run6) and  $(H/r)_{\text{out}} = 0.1$  (right, run7). The lower panels show each disc at a time of  $18 P_{\text{orb}}$ . The view is the  $x - y$  plane in which the planet orbits. In each panel, the red circle shows the planet with its size scaled to the size of the accretion radius. The star is along the positive  $x$  axis but is not shown on this scale. The colour of the gas denotes the column density with yellow being about two orders of magnitude larger than blue.

this simulation. The accretion rate is initially slightly lower than that of the higher  $\alpha$  simulation. During the high eccentricity phase of the KL oscillation, the accretion rate peak is similar. Thus the effect of lowering  $\alpha$  is to increase the lifetime of the disc. The disc is approaching a quasi-steady tilt that is close to the critical angle required for KL disc oscillations.

### 3 LONG TERM EVOLUTION OF THE SYSTEM

In this Section we discuss some effects that we have neglected in our simulations. We consider the effect of accretion on to the circumplanetary disc from the circumstellar disc, self-gravity of the circumplanetary disc and the spin-axis evolution of the planet.

#### 3.1 Accretion on to the circumplanetary disc

We have neglected the effect of accretion on to the circumplanetary disc from the circumstellar disc in all the simulations presented in this work. We estimate the effect of an accretion rate on to the disc,  $\dot{M}$ , by calculating the accretion timescale

$$t_{\text{acc}} = \frac{M_d}{\dot{M}} \quad (3)$$

(e.g. Pringle 1981). For typical parameters we find

$$\frac{t_{\text{acc}}}{P_{\text{orb}}} = 84 \left( \frac{M_d}{10^{-6} M_\odot} \right) \left( \frac{M_s}{1 M_\odot} \right)^{1/2} \left( \frac{a}{5.2 \text{ au}} \right)^{-3/2} \left( \frac{\dot{M}}{10^{-9} M_\odot \text{ yr}^{-1}} \right)^{-1}. \quad (4)$$

For these parameters, the accretion timescale is longer than the tilt timescale that is typically a few 10s of planet orbital periods. Once the disc is tilted, the accretion of material may occur at lower tilt angles and thus the tilt of the disc may be damped. We expect the disc to remain unstable to tilting but the timescale for the tilting may be longer than shown in our simulations. The accretion of circular orbit material into an eccentric disc that is undergoing KL oscillations does not necessarily suppress the instability (e.g. Smallwood et al. 2020).

#### 3.2 Circumplanetary disc self gravity

If a circumplanetary disc had sufficient mass to be self-gravitating, the dynamics of the disc may be changed. Strong self-gravity may be able to suppress KL disc oscillations (Batygin et al. 2011; Batygin 2012; Fu et al. 2017). The Toomre (1964) parameter is

$$Q = \frac{c_s \kappa}{\pi G \Sigma}, \quad (5)$$

where  $c_s = H\Omega$ ,  $\Omega = \sqrt{GM_p/r^3}$  and  $\kappa \approx \Omega$  is the epicyclic frequency. We take the initial surface density profile in our simulations

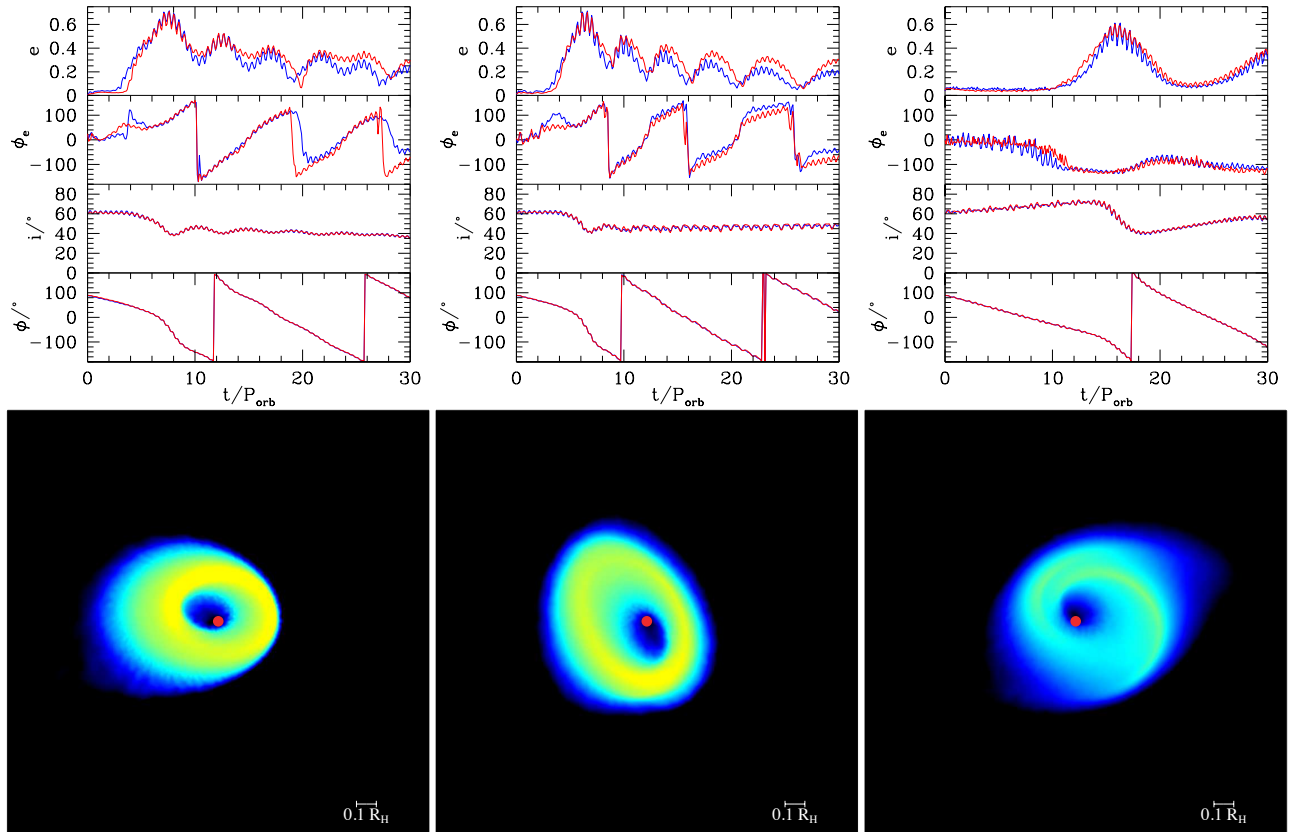


**Figure 6.** Same as Fig. 5 except the initial disc inclination is  $i_0 = 60^\circ$  with disc aspect ratio of  $(H/r)_{\text{out}} = 0.025$  (left, run8),  $H/r = 0.05$  (middle, run9) and  $H/r = 0.1$  (right, run10).

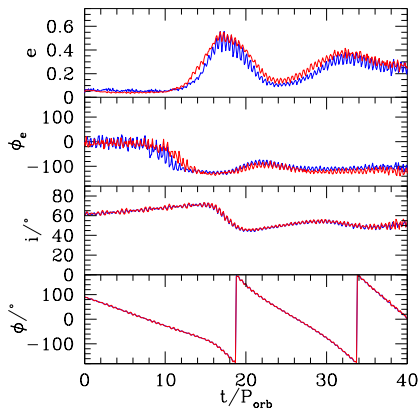


**Figure 7.** Same as the right panel of Fig. 6 (run10) except  $\alpha = 0.005$  (run11).

$\Sigma \propto r^{-3/2}$  with outer disc radius  $r_{\text{out}} = 0.4 r_H$ . The Toomre parameter is smallest at the outer disc edge. For  $(H/R)_{\text{out}} = 0.1$ , we find that for  $Q < 1.5$  the circumplanetary disc mass must be greater than  $0.2 M_p$ . Such a large disc mass may be prohibited from building up because spiral shocks transport angular momentum and enhance accretion on to the planet (Zhu et al. 2016; Chen et al. 2021). Thus, it is unlikely that KL oscillations in a circumplanetary disc can be suppressed by self-gravity.

Fu et al. (2017) found that a disc that undergoes KL oscillations may be able to fragment even though the disc is Toomre sta-

ble in the absence of KL oscillations. KL circumplanetary disc oscillations may be able to trigger the formation of satellitesimals. Gravitational instability within a protoplanetary disc is an alternative theory for giant planet formation in protoplanetary disc (Boss 1997) and may have similar implications for satellite formation in a circumplanetary disc. Gravitational instability can lead to disc fragmentation although the exact conditions required are still being actively researched (e.g. Papaloizou & Savonije 1991; Gammie 2001; Lodato & Clarke 2011; Paardekooper et al. 2011; Baehr & Klahr 2015; Kratter & Lodato 2016).

### 3.3 Planet spin axis evolution

The spin axis of a planet may be altered through two effects. First, it may change directly through misaligned accretion on to the planet from the inner edge of the circumplanetary disc. The angular momentum of the accreted material adds to the angular momentum of the planet. Since the mass of the circumplanetary disc is small compared to the mass of the planet, we expect this effect to be small. Secondly, the torque that a tilted disc exerts on a spinning oblate planet may change the planet spin-axis. This has been discussed before in the black hole case where the torque of a tilted disc aligns the black hole and the disc on a timescale that is much faster than accretion alone (e.g. Scheuer & Feiler 1996; Martin et al. 2007, 2009). We will investigate this in more detail in a future publication.

#### 4 DISCUSSION

The interplay of tilt and KL instability of circumplanetary discs has several potential implications. For the tilt mechanism to operate we have shown that the disc aspect ratio must be relatively large. This is expected for circumplanetary discs provided that the mass of the planet is lower than a threshold value. For a disc in a steady state, the disc aspect ratio scales with the planet mass as  $H/r \propto M_p^{-1/3}$ , with a weaker positive dependence on the planetary accretion rate (see equation 4 in [Martin & Lubow 2011](#)). Thus, the larger the planet mass, the smaller the disc aspect ratio. In the Solar System, different dynamics could therefore occur for Jupiter when compared to Saturn, Uranus and Neptune. We note that Jupiter has an equatorial plane that is close to aligned to its orbit, while the remaining giant planets are more highly misaligned.

Since regular satellites are thought to form in a circumplanetary disc, the eccentricity of the disc would affect their formation. In the protoplanetary disc case eccentricity due to the interaction of a close and eccentric binary companion may lead to destructive planetesimal collisions ([Paardekooper et al. 2008](#); [Kley & Nelson 2008](#); [Paardekooper & Leinhardt 2010](#); [Marzari et al. 2012](#)), hindering the the formation of planets ([Rafikov 2013](#); [Rafikov & Silsbee 2015a,b](#); [Silsbee & Rafikov 2015](#)). The presence of the gas disc can counteract this dynamical effect by providing a drag that is able to align the orbital eccentricities of the planetesimals, reducing the relative speeds of collisions ([Marzari & Scholl 2000](#)). The eccentricities experienced in a circumplanetary disc undergoing KL oscillation may be high,  $e \gtrsim 0.5$ . Regular satellite formation may need to proceed through different mechanisms in such highly eccentric discs. We also note that the threshold conditions for KL oscillations differ for gas discs and purely N-body systems. Solid bodies that form within a circumplanetary gas disc that is stable against KL oscillations may become unstable once the gas disc has dissipated if their inclination is above  $39^\circ$  (e.g. [Speedie & Zanazzi 2020](#)).

It is as yet unclear what will prove to be the best observational diagnostics of circumplanetary discs. Kinematic tracers provide powerful tools for characterizing eccentricities and misalignments in protoplanetary discs (e.g. [Bi et al. 2020](#)), and for testing the hypothesis that spirals, rings, and cavities within protoplanetary discs are caused by planets ([Muzerolle et al. 2010](#); [Zhu et al. 2011](#); [Zhang et al. 2018](#)). With sufficient sensitivity and spatial resolution, the distinctive kinematics of circumplanetary discs experiencing a phase of KL oscillations may be detectable. Currently, the indirect evidence pointing to a large disc-embedded planet population at large orbital radii is in some tension with direct imaging surveys that tend to suggest a smaller population, at least at high masses (e.g. [Bowler 2016](#)). Episodic accretion through a circumplanetary disc may be the cause of the low detection rate of accreting planets ([Brittain et al. 2020](#)). A circumplanetary disc that is undergoing KL oscillations would indeed undergo episodic accretion as shown in Fig. 3.

#### 5 CONCLUSIONS

Fluid discs around one component of a binary system that are sufficiently misaligned can be unstable to global KL disc oscillations ([Martin et al. 2014](#)). Furthermore, circumplanetary discs are linearly unstable to the growth of a disc tilt ([Lubow 1992](#); [Lubow & Ogilvie 2000](#); [Martin et al. 2020](#)). In this paper we have shown that detached circumplanetary discs have favourable disc

aspect ratios to become KL unstable after an initial phase of inclination growth due to the tilt instability. We have neglected accretion on to the circumplanetary disc that we expect to damp the tilt growth. However, for high enough disc aspect ratio,  $H/r \gtrsim 0.05$ , circumplanetary discs become misaligned on a short timescale and, provided that  $\alpha$  is sufficiently small and the disc lasts long enough, become KL unstable. A planet with a circumplanetary disc that is undergoing KL oscillations has episodic accretion that may explain the low detection rate of accreting planets. The eccentricity of the disc also has implications for regular satellite formation in the disc and the observability of circumplanetary discs and forming planets.

#### DATA AVAILABILITY STATEMENT

The results in this paper can be reproduced using the PHANTOM code (Astrophysics Source Code Library identifier [ascl.net/1709.002](https://www.ascl.net/1709.002)). The data underlying this article will be shared on reasonable request to the corresponding author.

#### ACKNOWLEDGEMENTS

We thank Daniel Price for providing the PHANTOM code for SPH simulations and acknowledge the use of SPLASH ([Price 2007](#)) for the rendering of the figures. Computer support was provided by UNLV's National Supercomputing Center. We acknowledge support from NASA TCAN award 80NSSC19K0639. CCY is grateful for the support from NASA via the Emerging Worlds program (Grant 80NSSC20K0347).

#### REFERENCES

- Akinsanmi B., Santos N. C., Faria J. P., Oshagh M., Barros S. C. C., Santerne A., Charnoz S., 2020, *A&A*, **635**, L8
- Alexander R. D., Clarke C. J., Pringle J. E., 2006, *MNRAS*, **369**, 216
- Andrews S. M., Wilner D. J., Hughes A. M., Qi C., Dullemond C. P., 2009, *ApJ*, **700**, 1502
- Ansdell M., et al., 2018, *ApJ*, **859**, 21
- Artymowicz P., Lubow S. H., 1996, *ApJ*, **467**, L77
- Ayliffe B. A., Bate M. R., 2009a, *MNRAS*, **393**, 49
- Ayliffe B. A., Bate M. R., 2009b, *MNRAS*, **397**, 657
- Baehr H., Klahr H., 2015, *ApJ*, **814**, 155
- Bate M. R., Bonnell I. A., Price N. M., 1995, *MNRAS*, **277**, 362
- Bate M. R., Bonnell I. A., Clarke C. J., Lubow S. H., Ogilvie G. I., Pringle J. E., Tout C. A., 2000, *MNRAS*, **317**, 773
- Bate M. R., Bonnell I. A., Bromm V., 2003, *MNRAS*, **339**, 577
- Batygin K., 2012, *Nature*, **491**, 418
- Batygin K., Morbidelli A., 2020, *ApJ*, **894**, 143
- Batygin K., Morbidelli A., Tsiganis K., 2011, *A&A*, **533**, A7
- Benz W., Slattery W. L., Cameron A. G. W., 1989, *Meteoritics*, **24**, 251
- Bi J., et al., 2020, *ApJ*, **895**, L18
- Boss A. P., 1997, *Science*, **276**, 1836
- Bowler B. P., 2016, *PASP*, **128**, 102001
- Brasser R., Lee M. H., 2015, *AJ*, **150**, 157
- Brittain S. D., Najita J. R., Dong R., Zhu Z., 2020, *ApJ*, **895**, 48
- Canup R. M., Ward W. R., 2002, *AJ*, **124**, 3404
- Chen C., Yang C.-C., Martin R. G., Zhu Z., 2021, *MNRAS*, **500**, 2822
- Clarke C. J., Gendrin A., Sotomayor M., 2001, *MNRAS*, **328**, 485
- D'Angelo G., Henning T., Kley W., 2002, *A&A*, **385**, 647
- Flaherty K. M., Hughes A. M., Rosenfeld K. A., Andrews S. M., Chiang E., Simon J. B., Kerzner S., Wilner D. J., 2015, *ApJ*, **813**, 99
- Flaherty K. M., et al., 2017, *ApJ*, **843**, 150
- Flaherty K. M., Hughes A. M., Teague R., Simon J. B., Andrews S. M., Wilner D. J., 2018, *ApJ*, **856**, 117



- Flaherty K., et al., 2020, *ApJ*, **895**, 109
- Franchini A., Martin R. G., Lubow S. H., 2019, *MNRAS*, **485**, 315
- Franchini A., Martin R. G., Lubow S. H., 2020, *MNRAS*, **491**, 5351
- Fu W., Lubow S. H., Martin R. G., 2015a, *ApJ*, **807**, 75
- Fu W., Lubow S. H., Martin R. G., 2015b, *ApJ*, **813**, 105
- Fu W., Lubow S. H., Martin R. G., 2017, *ApJ*, **835**, L29
- Fujii Y. I., Okuzumi S., Tanigawa T., Inutsuka S.-i., 2014, *ApJ*, **785**, 101
- Gammie C. F., 1996, *ApJ*, **457**, 355
- Gammie C. F., 2001, *ApJ*, **553**, 174
- Gressel O., Nelson R. P., Turner N. J., Ziegler U., 2013, *ApJ*, **779**, 59
- Hartmann L., Calvet N., Gullbring E., D’Alessio P., 1998, *ApJ*, **495**, 385
- Hueso R., Guillot T., 2005, *A&A*, **442**, 703
- Jontof-Hutter D., Lissauer J. J., Rowe J. F., Fabrycky D. C., 2014, *ApJ*, **785**, 15
- Katz J. I., Anderson S. F., Margon B., Grandi S. A., 1982, *ApJ*, **260**, 780
- Kley W., Nelson R. P., 2008, *A&A*, **486**, 617
- Kozai Y., 1962, *AJ*, **67**, 591
- Kratter K., Lodato G., 2016, *ARA&A*, **54**, 271
- Larwood J. D., Nelson R. P., Papaloizou J. C. B., Terquem C., 1996, *MNRAS*, **282**, 597
- Lidov M. L., 1962, *Planet. Space Sci.*, **9**, 719
- Lin D. N. C., Papaloizou J., 1986, *ApJ*, **309**, 846
- Lodato G., Clarke C. J., 2011, *MNRAS*, **413**, 2735
- Lodato G., Price D. J., 2010, *MNRAS*, **405**, 1212
- Lodato G., Pringle J. E., 2007, *MNRAS*, **381**, 1287
- Lubow S. H., 1992, *ApJ*, **398**, 525
- Lubow S. H., Martin R. G., 2012, *ApJ*, **749**, L37
- Lubow S. H., Martin R. G., 2013, *MNRAS*, **428**, 2668
- Lubow S. H., Ogilvie G. I., 2000, *ApJ*, **538**, 326
- Lubow S. H., Ogilvie G. I., 2017, *MNRAS*, **469**, 4292
- Lubow S. H., Seibert M., Artymowicz P., 1999, *ApJ*, **526**, 1001
- Lubow S. H., Martin R. G., Nixon C., 2015, *ApJ*, **800**, 96
- Lunine J. I., Stevenson D. J., 1982, *Icarus*, **52**, 14
- Martin R. G., Lubow S. H., 2011, *MNRAS*, **413**, 1447
- Martin R. G., Pringle J. E., Tout C. A., 2007, *MNRAS*, **381**, 1617
- Martin R. G., Pringle J. E., Tout C. A., 2009, *MNRAS*, **400**, 383
- Martin R. G., Nixon C., Lubow S. H., Armitage P. J., Price D. J., Doğan S., King A., 2014, *ApJL*, **792**, L33
- Martin R. G., Zhu Z., Armitage P. J., 2020, *ApJ*, **898**, L26
- Marzari F., Scholl H., 2000, *ApJ*, **543**, 328
- Marzari F., Baruteau C., Scholl H., Thebault P., 2012, *A&A*, **539**, A98
- Masuda K., 2014, *ApJ*, **783**, 53
- Millholland S., Batygin K., 2019, *ApJ*, **876**, 119
- Miranda R., Lai D., 2015, *MNRAS*, **452**, 2396
- Morbidelli A., Tsiganis K., Batygin K., Crida A., Gomes R., 2012, *Icarus*, **219**, 737
- Mosqueira I., Estrada P. R., 2003, *Icarus*, **163**, 198
- Muzerolle J., Allen L. E., Megeath S. T., Hernández J., Gutermuth R. A., 2010, *ApJ*, **708**, 1107
- Naoz S., 2016, *ARA&A*, **54**, 441
- Nixon C. J., 2012, *MNRAS*, **423**, 2597
- Nixon C., King A., Price D., 2013, *MNRAS*, **434**, 1946
- Owen J. E., Ercolano B., Clarke C. J., 2011, *MNRAS*, **412**, 13
- Paardekooper S. J., Leinhardt Z. M., 2010, *MNRAS*, **403**, L64
- Paardekooper S.-J., Thébault P., Mellema G., 2008, *MNRAS*, **386**, 973
- Paardekooper S.-J., Baruteau C., Meru F., 2011, *MNRAS*, **416**, L65
- Papaloizou J. C. B., Pringle J. E., 1983, *MNRAS*, **202**, 1181
- Papaloizou J. C., Savonije G. J., 1991, *MNRAS*, **248**, 353
- Papaloizou J. C. B., Terquem C., 1995, *MNRAS*, **274**, 987
- Pinte C., Dent W. R. F., Ménard F., Hales A., Hill T., Cortes P., de Gregorio-Monsalvo I., 2016, *ApJ*, **816**, 25
- Piro A. L., Vissapragada S., 2020, *AJ*, **159**, 131
- Price D. J., 2007, *Pasa*, **24**, 159
- Price D. J., Federrath C., 2010, *MNRAS*, **406**, 1659
- Price D. J., et al., 2018, *PASA*, **35**, e031
- Pringle J. E., 1981, *ARA&A*, **19**, 137
- Rafikov R. R., 2013, *ApJ*, **765**, L8
- Rafikov R. R., 2016, *ApJ*, **830**, 7
- Rafikov R. R., Silsbee K., 2015a, *ApJ*, **798**, 70
- Rafikov R. R., Silsbee K., 2015b, *ApJ*, **798**, 69
- Rogoszinski Z., Hamilton D. P., 2020, *ApJ*, **888**, 60
- Safronov V. S., 1966, *Soviet Ast.*, **9**, 987
- Scheuer P. A. G., Feiler R., 1996, *MNRAS*, **282**, 291
- Schulik M., Johansen A., Bitsch B., Lega E., Lambrechts M., 2020, arXiv e-prints, p. [arXiv:2003.13398](https://arxiv.org/abs/2003.13398)
- Shakura N. I., Sunyaev R. A., 1973, *A&A*, **24**, 337
- Silsbee K., Rafikov R. R., 2015, *ApJ*, **798**, 71
- Smallwood J. L., Lubow S. H., Franchini A., Martin R. G., 2019, *MNRAS*, **486**, 2919
- Smallwood J. L., Martin R. G., Lubow S. H., 2020, arXiv e-prints, p. [arXiv:2012.11068](https://arxiv.org/abs/2012.11068)
- Speedie J., Zanazzi J. J., 2020, *MNRAS*, **497**, 1870
- Szulágyi J., Morbidelli A., Crida A., Masset F., 2014, *ApJ*, **782**, 65
- Tanigawa T., Ohtsuki K., Machida M. N., 2012, *ApJ*, **747**, 47
- Terquem C. E. J. M. L. J., 1998, *ApJ*, **509**, 819
- Toomre A., 1964, *ApJ*, **139**, 1217
- Vokrouhlický D., Nesvorný D., 2015, *ApJ*, **806**, 143
- Ward W. R., Hamilton D. P., 2004, *AJ*, **128**, 2501
- Zanazzi J. J., Lai D., 2017, *MNRAS*, **467**, 1957
- Zhang S., et al., 2018, *ApJ*, **869**, L47
- Zhu Z., 2015, *ApJ*, **799**, 16
- Zhu Z., Nelson R. P., Hartmann L., Espaillat C., Calvet N., 2011, *ApJ*, **729**, 47
- Zhu Z., Ju W., Stone J. M., 2016, *ApJ*, **832**, 193